RSC Advances

PAPER

View Article Online
View Journal | View Issue

Cite this: *RSC Adv.*, 2024, **14**, 11715

Mechanism of cationic ring-opening polymerisation of ε-caprolactone using metallocene/borate catalytic systems: a DFT and NCI study on chain initiation, propagation and termination†

Wijitra Meelua,[ab] Mikko Linnolahti [c] and Jitrayut Jitonnom *[b]

We present a comprehensive DFT investigation on the cationic ring-opening polymerisation (CROP) of ε-caprolactone (CL) using zirconocene/borate catalyst systems. All possible pathways of the interaction between cationic species [Cp_2ZrMe^+] and counteranions, [A^-] = [$MeB(C_6F_5)_3]^-$ and [$B(C_6F_5)_4]^-$, were examined during chain initiation, propagation, and termination steps. The calculations reveal an active chain-end mechanism with *O*-alkyl bond cleavage of the polymerisation. The catalytic performance of the two counteranions is found to be identical, and they influence the initial process through stabilisation of the cationic species *via* non-covalent interactions (NCI), with the [$MeB(C_6F_5)_3]^-$ anion stabilising the catalyst–monomer complex more effectively than the [$B(C_6F_5)_4]^-$ anion by 24.3 kJ mol^{-1}. The first two propagations are likely the rate-determining step, with calculated free-energy barriers of 61.4–71.2 and 73.9–80.6 kJ mol^{-1} with and without the anions (A^-), respectively. The presence of the counteranion significantly affects the third propagation rate, lowering the barriers up to 20 kJ mol^{-1}. Comparison of the first termination and the third propagation shows that they are not competitive, with the termination being less facile. We also studied the initiation and propagation steps for the hafnocene catalyst and found that the Hf catalyst slightly favours the CL CROP in comparison to the Zr catalyst. Analysis of solvent and dispersion interaction demonstrates that both factors play an important role in the process. NCI analysis reveals weak (van der Waals) interactions at the contacts between the cationic species and the counteranions during the reaction course. Overall, our results offer insights into the structures and interactions involved in the polymerisation.

Received 15th February 2024
Accepted 1st April 2024

DOI: 10.1039/d4ra01178c

rsc.li/rsc-advances

1 Introduction

Polycaprolactone (PCL) is a popular biodegradable and biocompatible material that attracts industrial needs and has potential in biomedical and pharmaceutical applications.[1–3] Recently, PCLs have been a promising target towards functionalized polymers;[4,5] for example, they can be used as engineering plastics with high thermal stability and impact resistance. Synthesis of PCLs can be obtained from ring-opening polymerisation of cyclic esters, which is achieved by radical, anionic or cationic mechanisms,[6] through the ring opening of the cyclic monomer (Scheme 1).

A wide variety of catalysts/initiators have extensively been developed for the ring-opening polymerisation of cyclic esters.[7–11] Among them, Group 4 metallocene complexes are of particular interest in the synthesis of functionalized polymers, besides their well-known function as catalysts for olefin

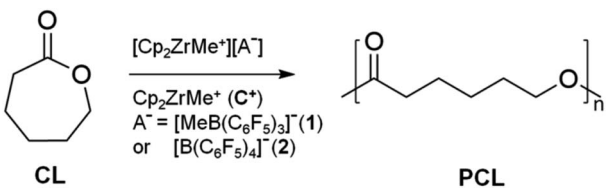

Scheme 1 Cationic ring-opening polymerisation (CROP) of ε-caprolactone (CL) using zirconocene/borate systems.

[a]*Demonstration School, University of Phayao, Phayao 56000, Thailand*
[b]*Unit of Excellence in Computational Molecular Science and Catalysis, and Division of Chemistry, School of Science, University of Phayao, Phayao 56000, Thailand. E-mail: jitrayut.018@gmail.com; jitrayut.ji@up.ac.th*
[c]*Department of Chemistry, University of Eastern Finland Joensuu Campus, Yliopistokatu 7, FI-80100 Joensuu, Finland*

† Electronic supplementary information (ESI) available: Gibbs free energy profiles resulting from two energetic correction Schemes I and II; validation of the chosen method; conformational analysis of CL and counteranions; charge analysis of ligands, monomer (CL), functional groups; data supporting the effects of metal and solvent; NCI results; cartesian coordinates (*XYZ*) of all optimised structures. See DOI: https://doi.org/10.1039/d4ra01178c

polymerisation.[12–14] In comparison with the metallocene-catalysed olefin polymerisation, there have been relatively few reports for the cationic ring-opening polymerisation (CROP) by these catalysts,[15] which makes them worthy of investigation.

Group 4 metallocene/borate catalytic systems[15] have been efficiently used in the cationic polymerisation of oxazolines,[16,17] vinyl ethers,[18] lactones,[19,20] cyclic carbonates,[21] and methyl methacrylate.[20] Current applications of these catalytic systems in polymer synthesis are, however, limited by their practical use, as they show less controlled molecular weight distribution (M_w/M_n), depending on many factors such as side reactions (unwanted species *e.g.*, aniline disrupts the catalyst performance, chain termination/chain transfer), concentration, and temperature. Besides, selecting appropriate catalyst/cocatalyst systems that match the polymerisation performance must be tested. Because of these practical limitations, understanding these catalytic processes would be the key for the design and improvement of the catalytic systems.

Two types of borate anions, methyltris(pentafluorophenyl) borate $[MeB(C_6F_5)_3]^-$ and tetrakis-(pentafluorophenyl)borate $[B(C_6F_5)_4]^-$, play a key role in the metallocene-mediated CROP reaction of cyclic esters and related monomers. These important species can be obtained *via* a catalyst activation using three different borate cocatalysts ($B(C_6F_5)_3$, $[B(C_6F_5)_4]^-[Ph_3C]^+$ and $[B(C_6F_5)_4]^-[Me_2NHPh]^+$): a cocatalyst abstracts a methide group from Cp_2ZrMe_2 to yield the ion-pair $[Cp_2ZrMe]^+[AMe]^-$ *via* ion-pair formation and separation steps. The final step separates the ion-pair species to produce a cationic species Cp_2ZrMe^+. The Cp_2ZrMe^+ is the active species in the polymerisation process and that the propagation occurs through the active chain-end (ACE) mechanism (Scheme 2),[22,23] where each propagating chain end featuring tertiary oxonium ions is initiated by a molecule of monomer, *e.g.* ε-caprolactone (CL).

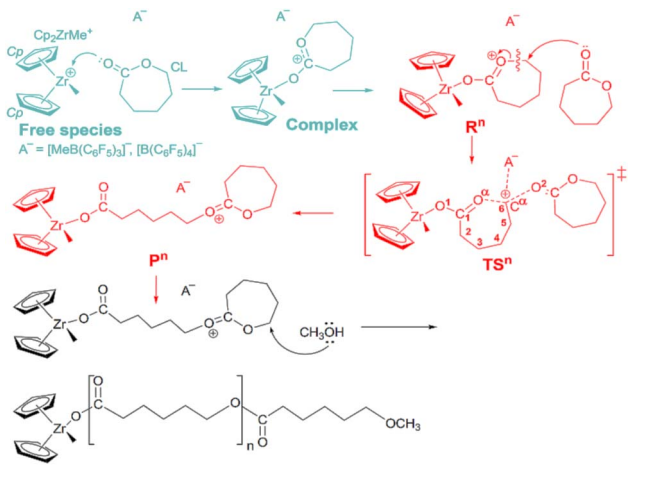

Scheme 2 Proposed mechanism for the CROP reaction with CL using catalytic $[Cp_2ZrMe^+][A^-]$ system (A^- = $[MeB(C_6F_5)_3]^-$ and $[B(C_6F_5)_4]^-$) showing species involved in the initiation (cyan), propagation (red) and termination (black) mechanism. Such species, including isolated cation and CL, monomer-activated complex, reactant, transition state and product, are labelled as Cp_2ZrMe^+, CL, complex, R^n, TS^n and P^n, respectively. Atomic definitions discussed in the text are also given in the figure.

Although the structural difference between the two anions is small, it is experimentally reported that polymerisation reaction by zirconocene catalyst with $[B(C_6F_5)_4]^-$ tends to provide different outcomes compared to that with $[MeB(C_6F_5)_3]^-$. For examples, Hayakawa *et al.* first utilized the well-known $[Cp_2ZrMe]^+[B(C_6F_5)_4]^-$ to initiate the living CROP of CL (affording PCL with narrow polydispersities, M_w/M_n = 1.06–1.3)[24] or cyclic carbonates such as 1,3-dioxepan-2-one.[21] Zirconium cations containing different methyl substituents on Cp ligand were used to polymerise the CL in toluene at room temperature or 60 °C.[19] The best catalytic system $[CpCp^*ZrMe]^+[B(C_6F_5)_4]^-$ was shown to polymerise CL with good control (M_w/M_n < 1.13, $M_{n,calcd} \approx M_{n,GPC}$), and the molecular weight of the resulting PCLs increased with monomer conversion. In 2007, Kostakis and co-workers[20] performed the CROP of CL and δ-valerolactone using three zirconocene complexes and three borate cocatalysts as initiation systems. Polymerisation of CL with $[Cp_2ZrMe]^+[MeB(C_6F_5)_3]^-$ reached a quantitative yield (>95% within 3–24 h at 25 °C) with very narrow polydispersity (M_w/M_n < 1.10), although experimental molecular weight higher than its theoretical value. Similar polymerisation results were also reported for the CROP of 1,5,7,11-tetraoxaspiro-[5,5]undecane, which was complete within 2 h at 55 °C with low polydispersity ($M_w/M_n \leq 1.2$).[25] On the contrary, the bulkier cocatalyst system $[Cp_2ZrMe]^+[B(C_6F_5)_4]^-$ polymerised CL in a controlled manner with agreement between calculated and observed molecular weight (yield >90% after 24 h at 25 °C). However, the molecular weights of the produced PCL can be varied (M_n = 10 000–38 000 g mol^{-1}) depending on the choice of zirconocene complex and cocatalyst. The same catalytic system was also used in the block copolymerisation with methyl methacrylate.

Similar distinct differences based on the two counteranions were also observed in CROP of poly(oxazoline)s:[17] the $[Cp_2ZrMe]^+[MeB(C_6F_5)_3]^-$ system gave a maximum yield of only 65% after 12.5 h while a quantitative polymerisation can be obtained in 5 h for the $[Cp_2ZrMe]^+[B(C_6F_5)_4]^-$ systems using $B(C_6F_5)_3$ or $[B(C_6F_5)_4]^-[Me_2NHPh]^+$ as cocatalysts. The same catalytic systems were also used in the synthesis of diblock copolymers and triblock terpolymers.[16,26] Overall, these experimental studies highlight the role of the counteranion in the CROP process and the polymerisation activity strongly depends on the bulkiness of the catalytic systems. In this study, we focus on the microscopic elucidation of the CROP reaction with CL in the presence of borate cocatalysts.

Theoretical studies have provided valuable insights into the reaction mechanism as well as elucidated factors (*e.g.*, counterion, solvent or metal) that are crucial for the metallocene-catalysed olefin and lactone polymerisations.[27] Most of the works have been carried out in the absence of cocatalyst and this simplified "naked cation" model[28,29] may not result in full understanding of the catalytic process. This is probably due to the size and conformational complexity of the ion-pair system,[30] so that theory and modelling could play an important role in this regard. Whereas numerous studies have focused on the effects of the catalyst structure using the naked model and the results have been interpreted in terms of a combination of steric and electronic effects, the molecular level details of the function

of the cocatalyst are not fully understood for the zirconocene catalysts. It is expected for metallocene/borate-mediated CROP that the effect of counteranions will be small, due to the weakly coordinating nature of F–H interaction of the cocatalyst as well as the diluted concentration of the dissociative counteranion caused by solvent and/or monomer during the reaction. Nevertheless, this hypothesis has never been verified in any previous studies.

Here, we first begin by modelling the reaction pathway of the chain initiation and propagation mechanism (Scheme 2) and identify the rate-determining step of the CL CROP reaction. Then, we examine the competitive reactions between the termination and the propagation. We analyse the effectiveness of both boron cocatalysts anions, $[MeB(C_6F_5)_3]^-$ and $[B(C_6F_5)_4]^-$, in the polymerisation with respect to the naked cation model lacking the anion. The influence of non-covalent interactions (NCIs) on the reaction kinetics of the process is further investigated by NCI analysis. The effects of metal, solvent, and dispersion interactions are also examined, and are found to be critical for the studied process.

2 Computational details

Geometries were fully optimised both in gas-phase and in solution using density functional theory (DFT)[31,32] at the B3LYP level with the Gaussian 09 program.[33] We used the effective core potential double-ζ basis set (LANL2DZ)[34] for Zr and Hf atoms and a double-ζ basis set, 6-31G(d), for all non-metal atoms (C, H, O, B, and F). This DFT/mixed basis set method has been widely used for transition metal complexes.[35–38] Vibrational frequency calculations were carried out to confirm the transition states and local minima obtained and to determine the zero-point vibrational energies (ZPE) and thermal corrections to the enthalpic (H) and Gibbs free energies (G) at standard temperature and pressure (298.15 K and 101.325 kPa). Geometry optimizations were also performed in toluene at the same level as the gas-phase optimised geometries, using the SMD/SCRF method[39] (toluene, $\varepsilon = 2.374$). Dispersion interactions were calculated using DFT-D3 method[40] with Becke–Johnson (BJ) damping scheme.[41] Thus, all reported energies account for zero-point, thermal, solvent and dispersion effects, unless noted otherwise. Population analysis (NBO, Mulliken and Hirshfeld charges) as implemented in Gaussian 09 was performed in gas-phase using the same functional and basis set as geometry optimizations. Here we have compared Gibbs free energies of species with differing numbers of molecules (*i.e.*, complex → **R1**, **P1** → **R2**, and **P2** → **R3**) using two energy correction schemes: the one where the reactants were completely isolated (named as "energy correction I") and the other one where the reactants were treated in the vicinity of each other (named as "energy correction II"), thus adopting the approach described by Gupta *et al.* for the metallocene/olefin systems.[42] The results of these two schemes are provided in Table S1 and Fig. S1 of ESI.† The energy correction II was used to produce the whole Gibbs free energy profiles for the studied CROP reaction.

The employed SMD(toluene)-B3LYP-D3(BJ)/LANL2DZ+6-31G(d) method was validated by comparison to a closely related reaction (Table 1), for which experimentally measured thermodynamic functions were available in toluene solution, together with X-ray geometry of the reactant.[43,44] The reaction enthalpy was reproduced by computations within a few-kJ mol^{-1}, while reaction entropy was overestimated, because the SMD/SCRF method does not consider the reduced translational entropy in solution. Using a Goodvibes script[45] modified to include molarity (9.4 mol dm^{-3}) and molecular volume (138.4 Å^3) of toluene,[46] we evaluated a correction to translational entropy (S-tr), as proposed by Whitesides *et al.*,[47] which brings the reaction entropy close to the experiment. However, the correction does not improve the prediction of reaction Gibbs energy because of the slight overestimation of reaction enthalpy. Benchmarking tests on computed reaction barriers with different DFT functionals and calculations of relative propagation energies (**R1**, **TS1** and **P1**) were also carried out, which further confirm that B3LYP-D3(BJ) is a suitable method for the current investigation as it provides the lowest barrier with a reasonable agreement in the calculated energetics between the employed method and the higher-level calculations (Fig. S2 and S3 of ESI†). Thus, the results of SMD(toluene)-B3LYP-D3(BJ)/LANL2DZ+6-31G(d) calculations are used for discussion throughout the study.

A conformational analysis was conducted to obtain the most stable configurations for the ion-pair model systems. In particular, different arrangements of CL monomer around the Zr centre at the complex were searched for the most stable geometry using a relaxed potential energy surface (PES) scan with the same level as geometry optimizations. During the scan, all the geometrical parameters were fully relaxed while the dihedral angle Me–Zr–C^1–O$^\alpha$ is varied in steps of 10° ranging from −180° to 180° (Fig. S4†). Points on the potential surface were then optimized, followed by frequency calculations to obtain various thermodynamic values. Once the stable complex structures (both *front* and *side* attacks) are located, the effect of the conformation of the counteranions ($[MeB(C_6F_5)_3]^-$ and $[B(C_6F_5)_4]^-$) around the Zr centre were evaluated for the catalytic species (complex → **P1**) (see Fig. S5 and S6 of ESI† for details).

Table 1 Theory *vs.* experiment for anti − $[(Cp''_2ZrMe)_2\mu - Me][MePBB] \leftrightarrow Cp''_2ZrMe_2 + [Cp''_2ZrMe][Me(PBB)]$[a]

Thermodynamic function[b]	B3LYP-D3(BJ)/LANL2DZ+6-31G(d)	Experimental
ΔE	56.9	
ΔH	47.6	42.9(8)
ΔS	148.2	110.7(17)
ΔG	3.5	10.1(2)
ΔS-tr[c]	101.9	110.7(17)
ΔG-tr[c]	17.3	10.1(2)

[a] Toluene solution, 298 K, Cp″ = η^5-1,2-Me$_2$C$_5$H$_3$, Me(PBB)$^-$ = $[MeB(ArF)_3]^-$ with ArF = *o*-(C$_6$F$_5$–C$_6$F$_4$). [b] ΔE, ΔH, and ΔG in kJ mol^{-1}, ΔS in J K^{-1} mol^{-1} with estimated standard deviation in parentheses. [c] Corrected for reduced translational entropy in solution.

To analyse the nature of interactions present between the cationic zirconocene species and the counteranions during the CL CROP, non-covalent interaction (NCI) analysis[48,49] is performed on important reaction intermediates and transition states using the NCIweb server (https://nciweb.dsi.upmc.fr/).[50] Contreras-Garcia *et al.* have recently introduced this user-friendly platform to study NCIs, based on the analysis of electron density, ρ, and reduced density gradient, s (also referred to as RDG), according to the eqn (1).

$$s = \frac{1}{2(3\pi)^{1/3}} \frac{|\nabla\rho|}{\rho^{4/3}} \quad (1)$$

In this NCIweb calculation, the promolecular density approximation is used,[51] and only an input structure (PDB, XYZ or WFN format) is required for each job submission. The final output files were provided by the NCI run *via* NCIplot code,[51] whereas 2D and 3D NCI isosurfaces were interactively visualised with JSmol. The NCI index helps identify and characterize weak interactions as chemically intuitive RDG isosurfaces, revealing both stabilizing (attractive interactions such as hydrogen bonding in blue, van der Waals interactions in green) and destabilizing interactions (repulsive clashes in red, weaker ones in yellow). The cutoff ($\rho = 0.3$ a.u.) is chosen to visualize the purely noncovalent interactions, unless otherwise specified.

3 Results and discussions

3.1 General consideration

The cationic polymerisation of cyclic esters with boron cocatalyst[15,19,20] generally consists of four complex steps: precatalyst activation, initiation, propagation, and termination. In the current study, we focus mainly on the initiation, propagation, and termination of CL CROP. Our goal is to explore mechanistic aspects of the CL CROP and try to understand the impact of the borate cocatalyst on the CROP activity of CL. We have previously shown that, by using a naked cation approach,[28,29] the first propagation is likely the rate-determining step of the CROP reaction.[37,52,53] However, to our best of knowledge, there is no systematic study in clarifying the influence of cocatalyst on the process. Here, three catalytic systems for CROP of CL have been modelled (Scheme 1): the first takes into account only the cationic zirconocene catalyst, Cp_2ZrMe^+, and CL monomer(s) (hereafter called the naked cation system, $\mathbf{C}^+$), while the second and third considered the $\mathbf{C}^+$ system in the presence of the cocatalyst anions ($A^- = [MeB(C_6F_5)_3]^-$ (**1**) and $[B(C_6F_5)_4]^-$ (**2**), respectively), which are the results of abstraction of one methyl group of the dimethylzirconocene, Cp_2ZrMe_2, yielding three different routes of catalyst activation (see eqn (2)–(4)).

$$Cp_2ZrMe_2 + B(C_6F_5)_3 \rightarrow Cp_2ZrMe^+ + [MeB(C_6F_5)_3]^- (\mathbf{1}) \quad (2)$$

$$Cp_2ZrMe_2 + [B(C_6F_5)_4]^-[Me_2NHPh]^+ \rightarrow Cp_2ZrMe^+ + [B(C_6F_5)_4]^- (\mathbf{2}) + Me_2NPh + CH_4 \quad (3)$$

$$Cp_2ZrMe_2 + [B(C_6F_5)_4]^-[Ph_3C]^+ \rightarrow Cp_2ZrMe^+ + [B(C_6F_5)_4]^- (\mathbf{2}) + Ph_3CMe \quad (4)$$

All model systems in the present work contain a 1 to 1 ratio of Zr : B, as experimentally reported by Hayakawa *et al.*[19] and Kostakis *et al.*[20] for lactone polymerisations using zirconocene/borate catalytic systems. The initiation, chain propagation, and termination mechanism is depicted in Scheme 2. All configurations of catalytic species found along the mechanism are provided in the ESI.† From the isolated reactants (Cp_2ZrMe^+ + CL + A^-; free species), the reaction starts with the insertion of the first CL monomer into the cationic site of Cp_2ZrMe^+, followed by the formation of a monomer-activated complex (Cp_2-ZrMe-CL$^+$, complex); hence this step is known as the "initiation" step. In the next step, the second CL monomer inserts into the C^{α}–O^{α} bond of the CL ring of the activated complex (**R1**) and generates a six-carbon polymer chain product (**P1**), through a transition state (**TS1**). This step is the first propagation step of the overall chain propagation. The next insertion of the third monomer and so on also follows the same process and continues until the quantitative polymer is obtained, once the growing chain end is terminated by a terminating agent (*e.g.*, methanol).[20]

We have organised our results into the following sections: we first examined the most favourable CROP pathway by considering possible configurations for the metallocene/borate model system. Second, we focus on the mechanism of chain initiation, propagation, and termination steps of the CL CROP reaction (Scheme 2), as promoted by three different catalytic systems ($\mathbf{C}^+$, $[C^+][MeB(C_6F_5)_3^-]$ (**1**), and $[C^+][B(C_6F_5)_4^-]$ (**2**)). Then, the effects of metal, solvent, and dispersion on the process were discussed. Finally, we identify and characterise weak interactions during the reaction course by means of NCI analysis.

3.2 Metallocene/borate models and possible CROP pathways

Presently, there are limited experimental data to support the initial configurations for the metallocene/borate catalytic systems $[Cp_2XMe^+][A^-]$ (X = Zr, Hf; $A^- = MeB(C_6F_5)_3^-$ and $B(C_6F_5)_4^-$) due to the probable dynamics of several species in solution.[46,54] Moreover, an experimental determination of toluene separated ion-pair for indenyl-based zirconocenes has recently been reported.[55] Therefore, current DFT calculations could allow us to gain insights into the structure and nature of active sites in metallocene/borate catalysts for cationic polymerisation of heterocyclic monomer.[15,56] To model the $[Cp_2XMe^+][A^-]$ system, in this study, we consider possible modes of CL coordination in combination with two different structures of the counteranions, $[MeB(C_6F_5)_3]^-$ and $[B(C_6F_5)_4]^-$. In the previous studies,[37,53] two different possible modes were considered for CL insertion into the cationic site of metallocene (namely *front* and *side* attack of CL; Scheme 3). Such insertion modes lead to the growing polymer chain in the *front* and *side* direction of the catalyst, respectively. A relaxed PES scan (Fig. S4†) was also performed in gas-phase for the complex between the *side* and *front* conformers, which are separated by a free-energy barrier height of 22 kJ mol^{-1} (Fig. S4(c), ESI†). This data indicates that both modes can be selective at least in the absence of counteranion at room temperature. For the [Cp_2-$ZrMe^+$][A^-] models, we first placed the counteranion in various

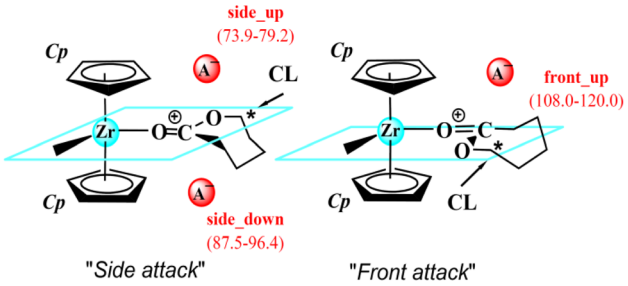

Scheme 3 Possible configurations for CL insertion mode and ion-pair interaction considered in the present study. Arrows indicate direction of CL insertion into the C–O bond of the monomer ring at the * position. Three distinct configurations of the anion (A^- = $[MeB(C_6F_5)_3]^-$ and $[B(C_6F_5)_4]^-$) with respect to the plane discussed in the current study (*side_up*, *side_down*, and *front_up*) were indicated with red spheres. Values are reaction barriers in units of kJ mol^{-1} calculated for each configuration discussed in this work.

positions around the metal centre of the catalyst (both complex and **P1**) and found that, after the conformational analysis (Fig. S5 and S6†), only three distinct configurations (*side_up*, *side_down*, and *front_up*) of the anion (see Scheme 3) were stably located, with respect to the plane of growing polymer chain in an extended conformation. Any configurations that lead to the coil polymer chain were excluded, since this would make the CL insertion inaccessible. Thus, eight different configurations were randomly selected (see Fig. 1 and Scheme 3): two for the naked cation system (*front* and *side*) and three (*side_up*, *side_down*, *front_up*) for the $[Cp_2ZrMe^+][A^-]$ systems.

As shown in Fig. 1, the *side* pathway is kinetically and thermodynamically favoured over the *front* pathway for all configurations. The free energies of complex relative to **R1** are in the ranges of 21.6–82.0 (*side*) and 56.7–70.7 (*front*) kJ mol^{-1}, whereas the reaction barriers and reaction free energies for the first propagation are in the ranges of 71.2–96.4 and 18.4–40.2 kJ mol^{-1} for the *side* pathway and 108.0–120.2 and 50.8–65.4 kJ mol^{-1} for the *front* pathway, respectively. For the naked cation (C^+) system, the *side* attack is kinetically favoured over the *front* attack by 41 kJ mol^{-1} and the relative stability of complex is 35.1 kJ mol^{-1} lower. For the $[Cp_2ZrMe^+][A^-]$ systems (**1** and **2**), the *side_up* configuration is favoured over the other two configurations (*side_down* and *front_up*) with the barrier differences of ~8–40 kJ mol^{-1} at **1-TS1** and ~22–34 kJ mol^{-1} at **2-TS1** in comparison with the *front_up* one, respectively. There is a significant difference in relative complexation energies and activation free energies between both *side_up* and *side_down* configurations of the anion systems. We thus selected the *side_up* instead of the *side_down* to represent the $[MeB(C_6F_5)_3]^-$ containing system **1** not only because of an energetic preference but also its equivalence in position and composition to the *side_up* of the $[B(C_6F_5)_4]^-$ containing system **2**, thus enabling direct comparisons. The optimised transition-state structures of the eight configurations are shown in Fig. 2. Apparently, the hydrogen bond (F–H) interactions between the cationic species and the counteranion lower free-energy barriers in the **R1** → **P1** step (see the *side* pathway in Fig. 1). Among them, the *side_up* configurations yield the lowest barriers of ~74–79 kJ mol^{-1} for both cocatalysts. Details of charge distribution of the ligand, monomer, functional groups on the free species, complex, **R1** and **TS1** structures for the *side_up* configurations are summarised in Tables S2 and S3 (ESI).†

Overall, the results clearly indicate that, for all catalytic systems, the *side* pathway is favoured for the CL polymerisation, which is in accordance with our previous studies for trimethylene carbonate (TMC) polymerisation catalysed by the naked cation species.[53] Thus, we focus on the initiation and propagation steps *via* the *side_up* pathway for the remaining study.

3.3 Exploring the mechanism of CL CROP

3.3.1 Chain initiation and propagation mechanism. We first investigate the chain initiation and propagation mechanism promoted by three Cp_2ZrMe^+/A^- systems, $[C^+][MeB(C_6F_5)_3]^-$ (**1**), $[C^+][B(C_6F_5)_4]^-$ (**2**), and the naked cation system C^+ (*i.e.*, in the absence of counteranion). The complete free energy profiles in toluene for the initiation and propagation mechanism of the systems (C^+, **1** and **2**) are shown in Fig. 3. Relative energies for the initiation and reaction barriers for the first, second and third propagation are collected in Table 2. The reaction starts with the insertion of the first CL molecule onto

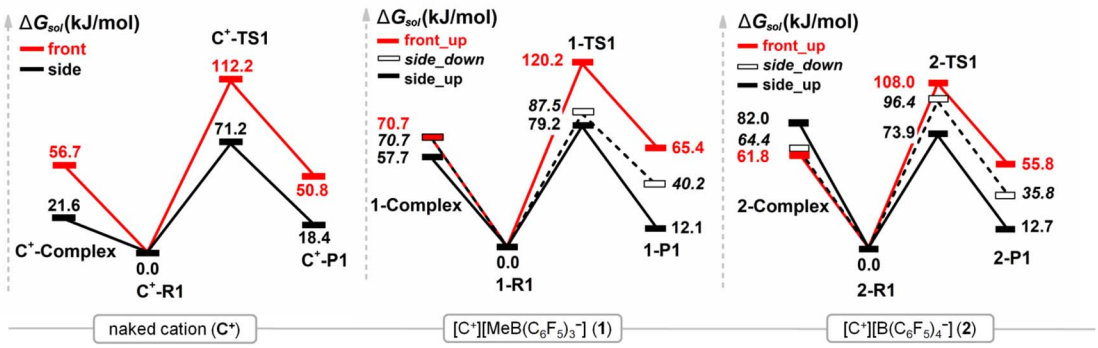

Fig. 1 Gibbs free energy profiles in toluene for the initiation and first propagation for various reaction pathways for the naked cation (C^+), $[C^+][MeB(C_6F_5)_3^-]$ (**1**) and $[C^+][B(C_6F_5)_4^-]$ (**2**) systems. The Gibbs energy of each structure is given relative to the reactant of the first propagation (**R1**). All of the stationary structures shown in this figure are provided in the ESI.†

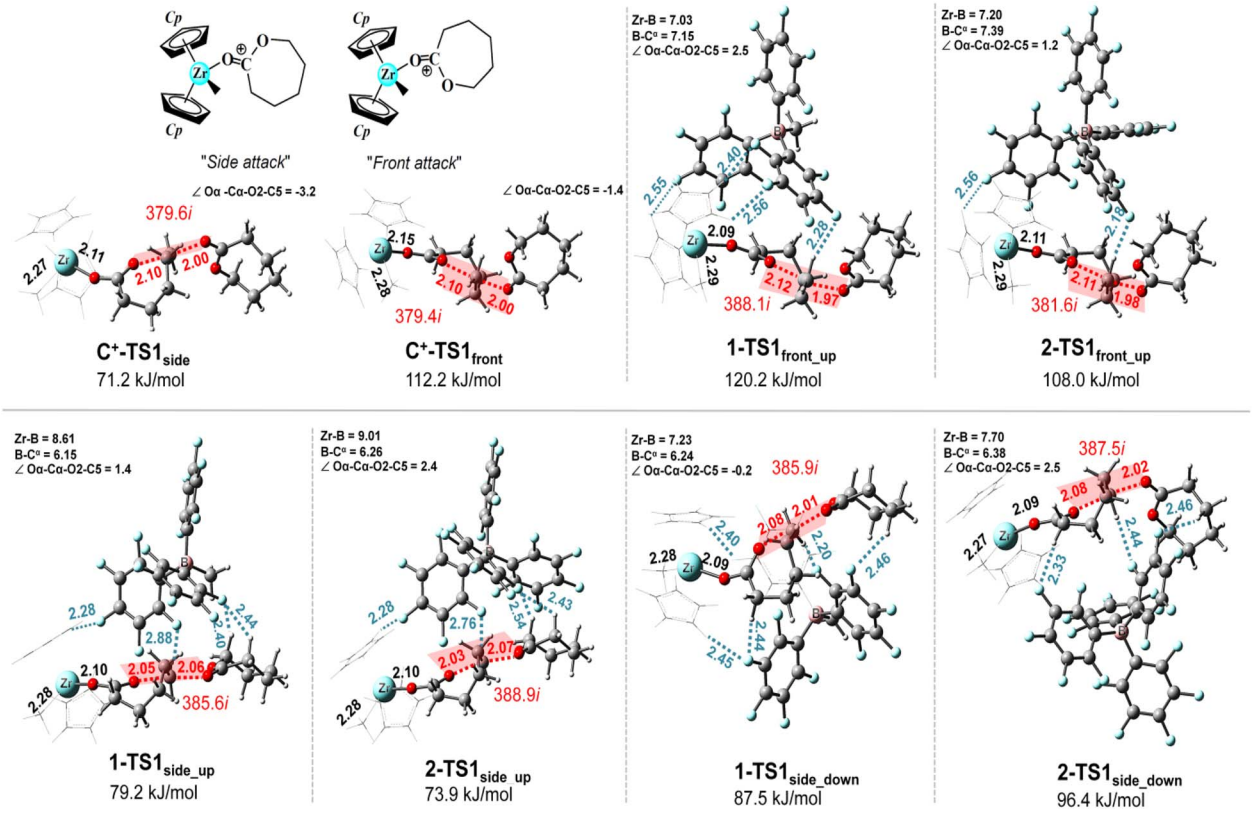

Fig. 2 Optimised transition-state structures (**TS1**, distances in Å) and their corresponding activation energies (free energies in kJ mol^{-1}) relative to **R1** for the eight configurations in Fig. 1. Imaginary frequencies (in cm^{-1}) are also indicated. A small torsional angle (in deg.) of O^{α}–C^{α}–O^{2}–C^{5} ≈ 0–3 deg. represents a planar alignment of the four-centred transition states. Other planes were also seen for further chain propagations (see ESI†). Hydrogen bond (F–H) interactions between the cationic species $\mathbf{C}^+$ and the counteranion are indicated by the dotted line.

the central metal of Cp_2ZrMe^+ and leads to the monomer-activated complex $[Cp_2ZrMe\text{-}CL]^+$ (complex), which is then active towards the insertion of the second monomer, setting the initial stage for the chain propagation (**R1**). This initiation step is essentially electrostatic in nature, and is exergonic by −69.7, −109.3, and −85.0 kJ mol^{-1} for free species → complex and −91.3, −167.0, and −167.0 kJ mol^{-1} for free species → **R1** of the $\mathbf{C}^+$, **1** and **2** systems, respectively. These negative energies further support that the initiation is a spontaneous process. The data also indicates that the $[MeB(C_6F_5)_3]^-$ anion effectively stabilises the activated complex by 24.3 kJ mol^{-1} (−85–(−109.3) = 24.3 kJ mol^{-1}, Table 2) with respect to the $[B(C_6F_5)_4]^-$ anion. This is associated with weaker repulsive clashes detected in the NCI analysis for **1**-complex ($\int\rho(r)dr = 36.5$ for **1**-complex *vs.* 40.7 for **2**-complex at the [0.02, 0.1] range, see Fig. S12 and S13 of ESI† for details). For the chain propagation, the first three propagation steps were considered, and their relative energy profiles were compared to determine the overall propagation rate. As shown in Fig. 3, for all catalytic systems, the relative energies of all propagating species are largely decreased as the polymer chain grows, indicating the living polymerisation.[22,23] The reaction barriers as estimated for the first, second, and third propagation steps, respectively, are 71.2, 61.4, and 69.2 kJ mol^{-1} for $\mathbf{C}^+$ and 79.2, 80.6 and 62.0 kJ mol^{-1} for **1** and 73.9, 78.2, and 61.1 kJ mol^{-1} for **2** (Table 2). These results reveal that the reaction barriers for the first three propagations have no significant discrepancy between the systems **1** and **2** (62.0–80.6 *vs.* 61.1–78.2 kJ mol^{-1}, respectively), suggesting that the effect of adding two distinct counteranions was identical in the chain propagation. This is also evident by similar non-covalent interactions detected in the 2D and 3D isosurfaces below. Despite little difference is seen for the studied chain propagation of the $[\mathbf{C}^+][A^-]$ systems (**1** and **2**), both cocatalyst anions appear to stabilise the cationic species immediately after the first CL is opened (after **TS1**, see ΔG_{sol} for $\mathbf{C}^+$ *vs.* **1** and **2** in Fig. 3). Note that the barriers of the third propagation for both cocatalysts are significantly reduced to ∼60 kJ mol^{-1} (Table 2), which may be attributed to more extensive H-bond interactions between the cationic growing site and the cocatalyst, as compared to the cases of the first two propagation steps (Fig. 4). Since the first and second propagation steps showed the highest and comparable barriers (79.2–80.6 and 73.9–78.2 kJ mol^{-1} for **1** and **2**, respectively), they are likely the rate-determining step of the studied process. These barriers are lower in $\mathbf{C}^+$ (61.4–71.2 kJ mol^{-1}), which demonstrate that the polymerisation must occur more readily without the counteranions.

The optimised transition-state structures in toluene for the first three propagations (**TS1**, **TS2**, **TS3**) are shown in Fig. 4. All configurations of the stationary points (free species, complex, $\mathbf{R}^n$, $\mathbf{TS}^n$, $\mathbf{P}^n$; $n = 1$–3) are given in the ESI.† Using its fluorides, the

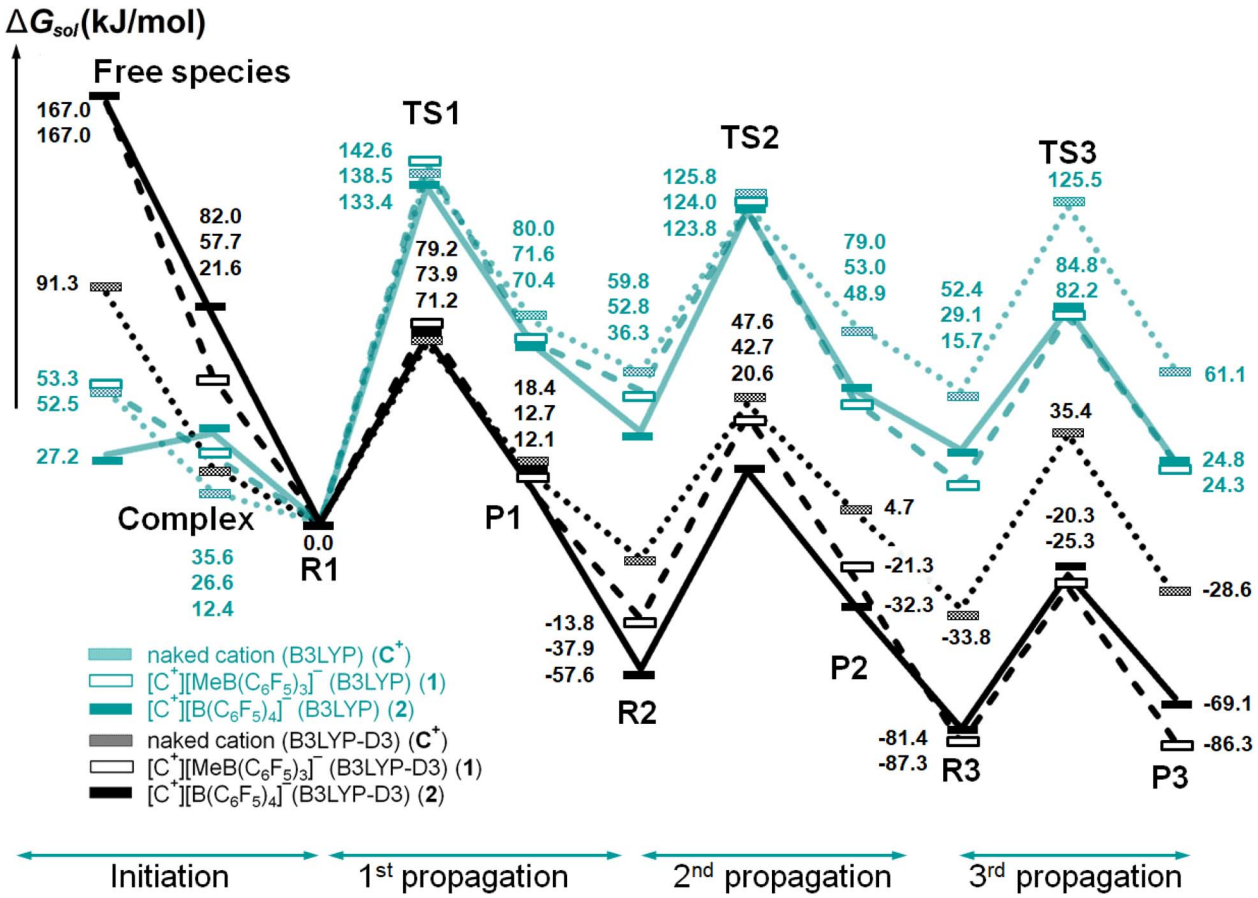

Fig. 3 Gibbs free energy profiles in toluene (shown in black) for the initiation and propagation mechanism of the three catalytic systems (C^+, **1**, and **2**). The uncorrected free energy profiles for the dispersion interaction were also included for comparison (shown in cyan). Relative barrier heights for each of propagation steps were also included in Table 2.

Table 2 Relative energies for the initiation and reaction barriers (ΔG in kJ mol^{-1}) for the first, second and third propagation shown in Fig. 3 and the first termination shown in Fig. 5 for three catalytic systems (C^+, **1**, and **2**)[a]

Reaction steps	C^+	1	2
Initiation (free species → complex)	−69.7	−109.3	−85.0
First propagation (**R1** → **TS1**)	71.2	79.2	73.9
Second propagation (**R2** → **TS2**)	61.4	80.6	78.2
Third propagation (**R3** → **TS3**)	69.2	62.0	61.1
First termination ($\mathbf{R3}^{ter}$ → $\mathbf{TS3}^{ter}$)	85.1	55.9	74.5

[a] Toluene solution, 298 K.

cocatalyst forms hydrogen-bond (H-bond) interactions with the methylene atoms at the C^{α} position, facilitating the chain propagation. At **TS1**, due to the spatial separation, only C^{α} atom can directly interact with the $-C_6F_5$ ring of the cocatalyst (see distance *c*, Fig. 4a and b), with **1** being shorter than **2** (2.55 *vs.* 2.90 Å, respectively). This F–H interaction limits the formation of the first transition state and hence a relatively higher barrier at **TS1** is observed for **1** compared to that for **2** (79.2 *vs.* 73.9 kJ mol^{-1}). However, in the second and third propagations (**TS2** and **TS3**), the $-C_6F_5$ ring of the cocatalyst ring can effectively stabilise the growing reactive species, as can be seen from the more numerous H-bond interactions (distances c–e). At **TS3** of both systems, the incoming monomer interacts with two H-bonds, but the $-C_6F_5$ rings of the $[B(C_6F_5)_4]^-$ cocatalyst form more numerous F–H interactions with the ancillary Cp ligand of the metallocene, as well as with the growing chain, in comparison to the case of the $[MeB(C_6F_5)_3]^-$ anion (see **TS3** in Fig. 4). These interactions are consistent with more van der Waals contacts between the cationic zirconocene species and the counteranion revealed by the NCI analysis below.

Comparing the activation energies of the first propagation obtained using the naked model in this work (71.2 kJ mol^{-1}) with the data reported in the literature, it was found that the CROP reaction with CL has a faster propagation step compared to zirconocene-initiated TMC propagation (115.9 kJ mol^{-1})[53] and methyl tosylate-initiated propagation with 2-R-2-propyl-oxazoline (R = cyclopropyl, *n*-propyl, isopropyl) (95–110 kJ mol^{-1}).[57]

3.3.2 Chain termination mechanism. To further examine whether the chain termination possibly competes with the third propagation step, we used the same procedure as in the chain propagation to model the first termination step after intermediate **P2** using methanol (CH_3OH), a common terminating

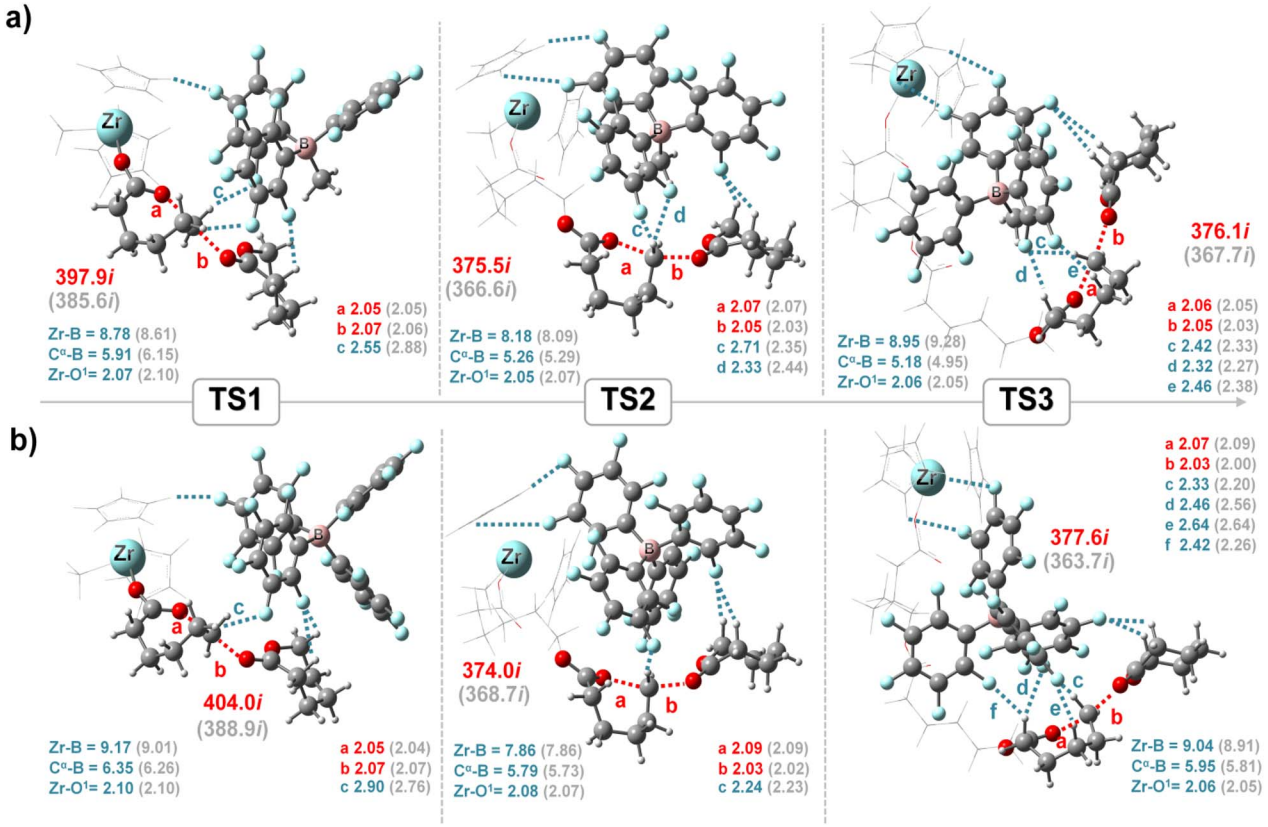

Fig. 4 Optimised transition-state structures in toluene for the first three propagation steps (**TS1**, **TS2**, **TS3**) for $[C^+][MeB(C_6F_5)_3]^-$ (a) and $[C^+][B(C_6F_5)_4]^-$ (b). Gas-phase results (imaginary frequencies and geometries) for the corresponding transition states are also included in parenthesis. Bonds being formed and broken are shown by alphabet letters (a and b) and in red dotted lines. Hydrogen bond interactions are indicated with alphabet letters (c–e) and cyan dotted lines.

agent that has been used experimentally.[20] Here, the zirconocene system was considered. The reaction barriers, relative Gibbs energies, and optimised structures of reactant, transition states, and product (denoted as $\mathbf{R3}^{ter}$, $\mathbf{TS3}^{ter}$, and $\mathbf{P3}^{ter}$) in toluene for the termination of systems **1** and **2** are depicted in Fig. 5 and Table 2, in comparison with those of the third propagation. During the first three propagations between the three catalytic systems, we encountered a chain termination for system **1** due to a lower calculated barrier at $\mathbf{TS3}^{ter}$ compared to the third propagation (55.9 *vs.* 62.0 kJ mol^{-1}, respectively). This is further supported by stronger attractive interactions in the $[MeB(C_6F_5)_3]^-$ system at **1**-$\mathbf{TS3}^{ter}$ (see Fig. S14–S16† for a marked difference between **TS3** and $\mathbf{TS3}^{ter}$). However, the termination process is unlikely to compete with the third propagation step for the systems $\mathbf{C}^+$ and **2** (85.1 *vs.* 69.2 kJ mol^{-1} and 74.5 *vs.* 61.1 kJ mol^{-1}, respectively). Notably, the relative Gibbs energies of the termination step are greatly lowered in the presence of the cocatalysts, but still being less facile (1.4 and 6.5 kJ mol^{-1} at $\mathbf{TS3}^{ter}$ for **1** and **2**) compared to that of the third propagation step (−25.3 and −20.3 kJ mol^{-1} at **TS3** for **1** and **2**). For most cases, the third propagation is kinetically and thermodynamically favoured over the termination and the counteranions greatly stabilise the terminating species after the first CH_3OH insertion at the reactive chain end, especially at **P3** (decreasing from 43 kJ mol^{-1} for $\mathbf{C}^+$ to −47.5 and −92.0 kJ mol^{-1} for **1** and **2**). However, the stable product **P3** that is formed after the **TS3** of the $[B(C_6F_5)_4]^-$ containing system (**2**) also indicates that the termination is thermodynamically driven, with **2** being more feasible than **1** (−92.0 *vs.* −47.5 kJ mol^{-1}).

3.3.3 Effects of metal, solvent and dispersion interaction. The initiation and propagation mechanism is also studied with hafnocene catalyst, Cp_2HfMe^+, in comparison to zirconocene catalyst systems for both anions, $[MeB(C_6F_5)_3]^-$ and $[B(C_6F_5)_4]^-$. The results are included in Fig. S7.† The Gibbs energy barriers of the rate-determining step (**R1** → **TS1**) are 67.7 and 71.2 kJ mol^{-1} with hafnocene in comparison to the 79.2 and 73.9 kJ mol^{-1} with zirconocene for $[MeB(C_6F_5)_3]^-$ and $[B(C_6F_5)_4]^-$, respectively. Generally, the reaction is systematically more exergonic for the hafnocene than for the zirconocene, and the energetic difference between the Zr and Hf systems becomes evident for successive CL insertion in the presence of cocatalysts (Fig. S7, ESI†). Thus, the hafnocene catalyst significantly favours the CL CROP compared to the zirconocene catalyst, with the effect becoming more pronounced after the first CL is opened. The higher activity of Hf over Zr is associated with significant decreases in positive charges on the central metal (qHf = 0.771e − 0.828e *vs.* qZr = 0.792e − 0.846e for Mulliken charges in **2**) and metal–ligand

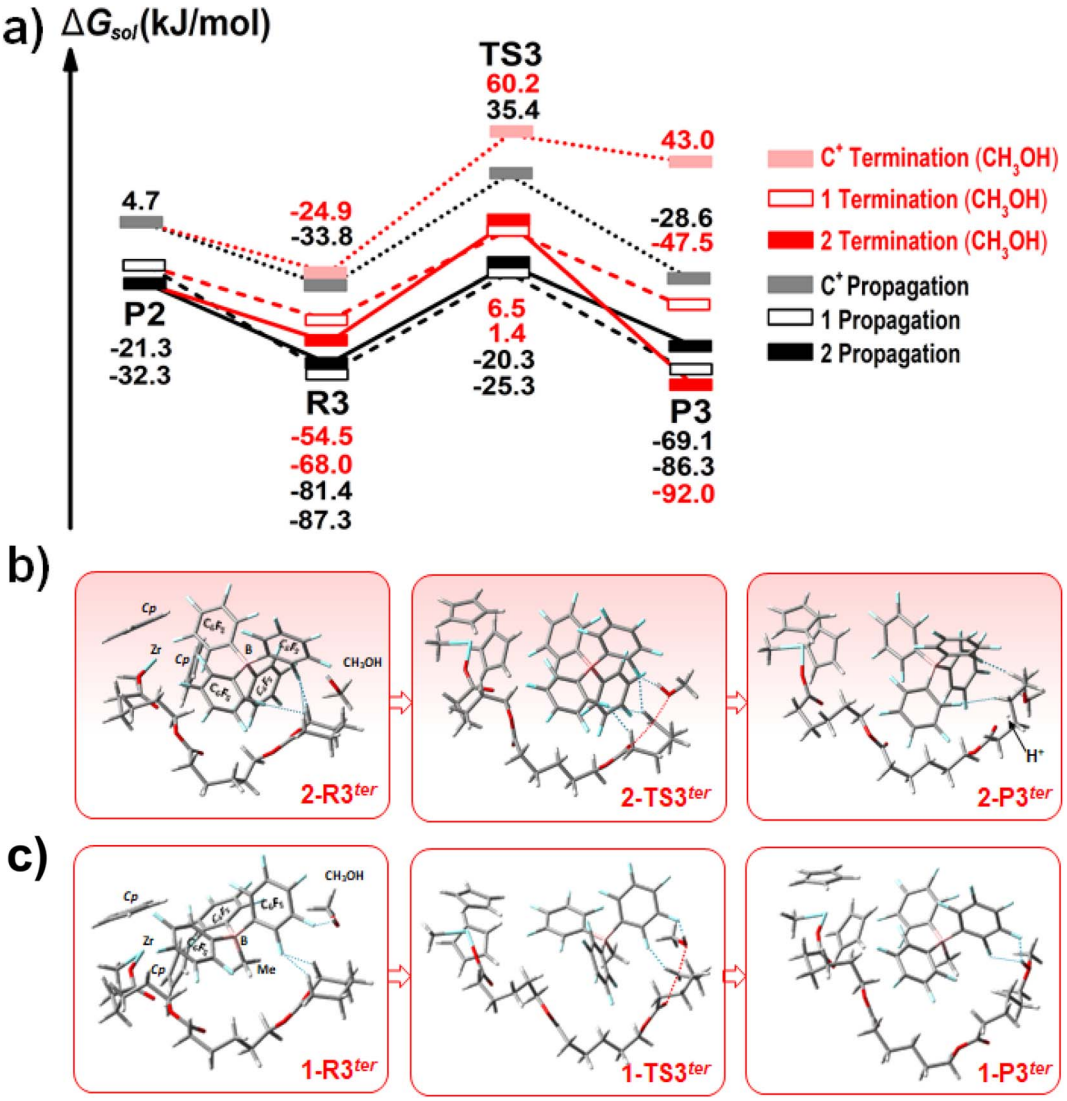

Fig. 5 (a) Gibbs free energy profiles in toluene for the third propagation and first termination mechanism of the three catalytic systems (C^+, **1**, and **2**) using zirconocene catalyst Cp_2ZrMe^+. (b and c) Toluene-optimised structures of (b) **2-R3**^{ter}, **2-TS3**^{ter}, **2-P3**^{ter} and (c) **1-R3**^{ter}, **1-TS3**^{ter} and **1-P3**^{ter} for the termination in systems **2** and **1**, respectively.

distances along the reaction pathway (Hf–O^1 = 2.010–2.121 Å, Hf–Me = 2.253–2.266 Å *vs.* Zr–O^1 = 2.051–2.175 Å, Zr–Me = 2.278–2.292 Å for distances in **2**) (see Fig. S8 and Table S4†). The same trend can also be seen in **1**.

The solvent effect is addressed by a comparison between the Gibbs energy profiles in toluene solution with the gas-phase Gibbs energy profiles (Fig. S9†). Generally, the toluene Gibbs energy profiles show a similar trend as in the gas-phase. Interestingly, the solvent clearly destabilises the catalytic species, thus increasing the reaction barriers and relative energies of the propagating intermediates (cyan lines, Fig. 3). The reaction barriers of the first propagation for systems C^+, **1**, and **2** are 138.5, 142.6, and 133.4 kJ mol^{-1} in toluene, in comparison to the corresponding values, 85.8, 73.0, and 74.8 kJ mol^{-1} in gas-phase, respectively (Fig. S9†). The notable decrease in the complex stability, and the higher energy profile for chain propagation, indicate that the solvent largely disfavours both initiation and propagation steps. The initiation is even kinetically disfavoured for the case of $[B(C_6F_5)_4]^-$, with a small barrier of 8.4 kJ mol^{-1} for the free species → **R1** step (Fig. 3). Electronically, the LUMO energies, HOMO–LUMO gaps, and Mulliken charges on the Zr atom along the reaction pathway are relatively higher in toluene solution compared to the gas-phase (Fig. S10 and Table S5, ESI†). Overall, the solvent favours the separation of the ion species, rather than stabilising the ion pair.

Besides showing the importance of the solvent effect, we demonstrate in the following that the dispersion interactions are important, as well. The dispersion corrected Gibbs energy profiles in toluene solution for the three catalytic systems (C^+, **1**, and **2**) are compared to the corresponding uncorrected results in Fig. 3. The barriers for the first propagation step (**R1** → **TS1**) range between 133.4–142.6 and 71.2–79.2 kJ mol^{-1} for the uncorrected and corrected free energy profiles, respectively. The

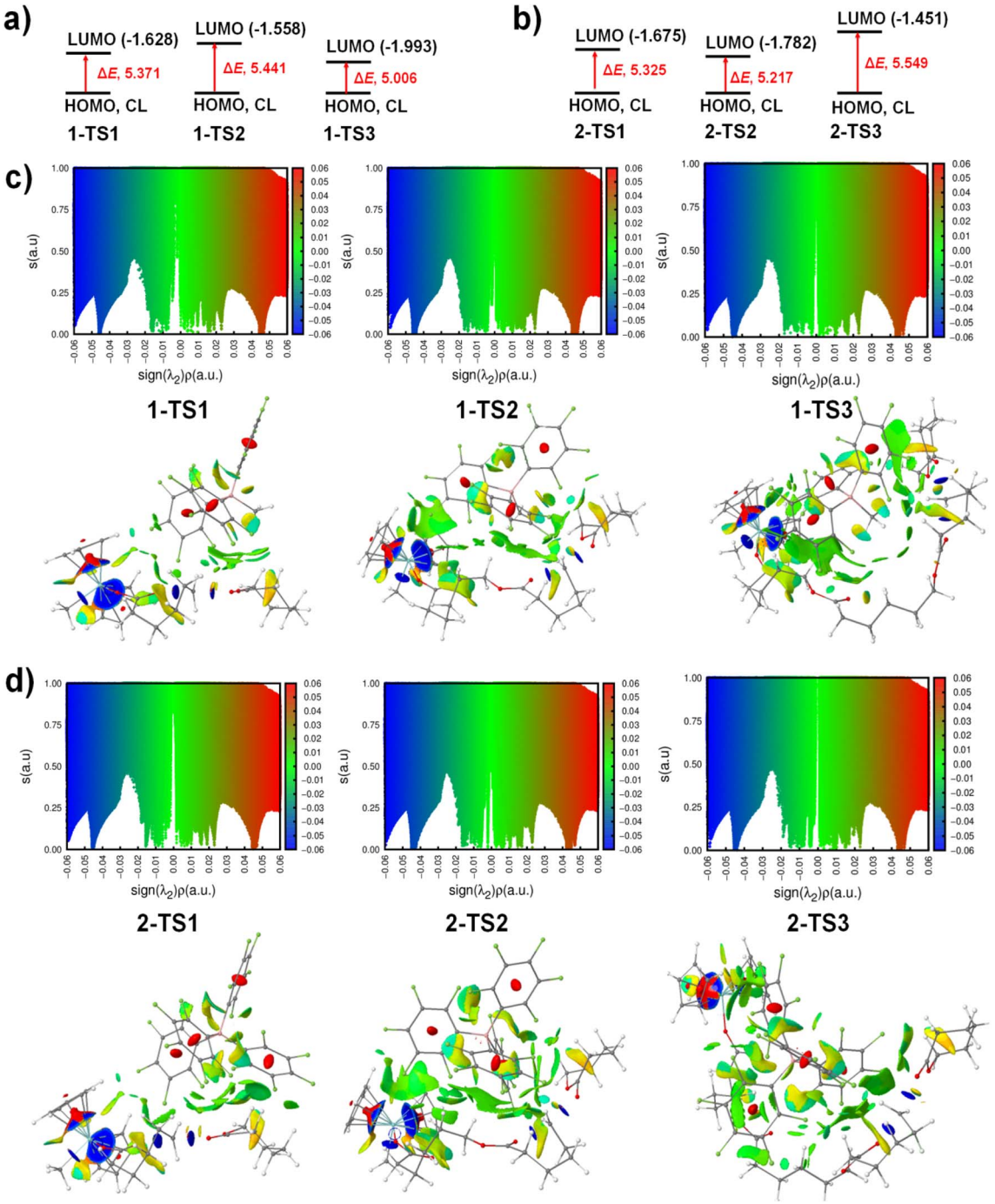

Fig. 6 (a and b) HOMO–LUMO gaps (Δ*E*, eV) and (c and d) NCI analysis of computed transition states in the chain propagation. (a and b) The HOMO–LUMO energy gaps were obtained as the difference between the HOMO energy of the CL monomer (−7.000 eV) and the LUMO energies of the transition states of the zirconocene/borate systems **1** (a) and **2** (b). (c and d) 2D (upper) and 3D (lower) isosurfaces of the transition-state structures (**TS1**, **TS2**, **TS3**) calculated for the first three propagation steps of the systems **1** (c) and **2** (d). Toluene-optimised geometries were used as inputs for this NCI analysis using promolecular density. The NCI isosurfaces ($s = 1.0$ a.u. for 2D and 0.3 a.u. for 3D, -0.06 a.u. < sign(λ_2)ρ < 0.06 a.u.) are coloured in blue, green, and red isosurfaces, respectively (atom colour code: light gray, C; dark blue, N; white, H; red, O; pink, B; green, F; cyan, Zr).

results clearly indicate that the catalytic species are greatly stabilised by the multitude of noncovalent interactions involved in the system, which clearly cannot be omitted in the calculations. With dispersion interactions included, the overall Gibbs energy reaction profile ends up exergonic, as it needs to be for a spontaneous reaction.

These results altogether indicate that both solvent and dispersion effects are important for the CROP mechanism: solvent destabilises the reaction intermediates, whereas

dispersive interactions strongly stabilise them. Thus, the overall propagation rate of the three catalytic systems is likely dictated in the initial stage of the chain propagation, in accordance with a similar study on the ROP of 1,5,7,11-tetraoxaspiro[5,5]undecane using $[Cp_2ZrMe^+][MeB(C_6F_5)_3^-]$.[25]

3.4 NCI analysis

Non-covalent interactions play a crucial role in the stability and reactivity of organometallic systems.[58] To gain a deeper insight into the non-covalent interactions (NCIs) that influence the dispersion effect and F–H interactions during the reaction course, the intramolecular NCIweb calculations of intermediates and transition-state structures were performed. A pictorial representation of NCI isosurfaces in 2D and 3D for the transition states (**TS1**, **TS2**, and **TS3**) in chain propagation is shown in Fig. 6, with the HOMO–LUMO gaps included for comparison. The NCI results for other intermediates and integrals of electron density can be found in the ESI.† The 2D NCI plots are almost identical for all catalytic species and highlight three distinct NCI regions of attractive (blue), van der Waals (green), and repulsive (red) non-covalent interactions (Fig. 6c, d and S12†). Two blue peaks of localized and attractive (electrostatic) interactions appear at higher negative values of $\mathrm{sign}(\lambda_2)\rho$ on the 2D-RDG: the sharp and low-density peak (at $\mathrm{sign}(\lambda_2)\rho = -0.06$ a.u.) corresponds to the transient C^{α}–O^{α}/C^{α}–O^2 bonds and the Zr–Me/Zr–O^1 bonds, with blue and donut-shaped isosurfaces, and the wider one at greater densities appears between $\mathrm{sign}(\lambda_2)\rho = -0.04$ and -0.05 a.u., which corresponds to the strong attractive interactions between the Zr atom and the Cp ligands (the large blue 3D isosurfaces on catalyst, see lower panels in Fig. 6c and d). At higher positive values of $\mathrm{sign}(\lambda_2)\rho$, in red, we recognise the repulsive interaction regions inside the $-C_6F_5$ rings of counteranions, shown in red compact isosurfaces. A green wider NCI region on 2D-RDG, at both negative and positive scales of $\mathrm{sign}(\lambda_2)\rho$, indicates the existence of delocalized and van der Waals (vdW) interactions, which corresponds to green isosurfaces at the contacts between the cationic zirconocene species and the counteranion. The similarity of the 2D-RDG spectra in all TSs (upper panel, Fig. 6c and d) also explain the same kinetic behaviours observed in Table 2 for the chain propagation between the two cocatalyst systems. Notably, two attractive and vdW interactions are primarily observed at the reactive chain end, facilitating the stabilization of the developing positive charge (C^{α}) in the transition states. This provides an evidence for the roles of multiple NCIs in transition-state charge stabilization in CROP.[59]

Despite the fact that both cocatalyst systems show the same interaction types, their HOMO–LUMO properties and interaction strengths differ significantly as the reaction progresses. The HOMO–LUMO gaps (ΔE) decrease in the $[MeB(C_6F_5)_3]^-$ anion ($\Delta E = 5.371$ eV at **1-TS1** to 5.006 eV at **1-TS3**), while $[B(C_6F_5)_4]^-$ shows opposite trends (see Fig. 6a and b). Interestingly, the LUMO energies at TSs are strongly influenced by the NCIs: $[MeB(C_6F_5)_3]^-$ effectively stabilises the **TS3** with a lower E(LUMO) value (-1.993 eV) compared to that in $[B(C_6F_5)_4]^-$ (E(LUMO) $= -1.451$ eV). These energy gaps also correlate well with the transition-state barriers ($R^2 = 0.99$) (Fig. S17†). Since the interaction strengths can be quantitatively estimated from the integration of electron density (see $\int\rho(r)\mathrm{d}r$ in Fig. S18†), we recognised that, from **TS1** to **TS3**, the strength of attractive vdW interactions becomes stronger (with higher $\int\rho(r)\mathrm{d}r$ values) and, due to the larger size, $[B(C_6F_5)_4]^-$ creates more contacts with the cationic species and hence stronger dispersion forces between them, as compared to the $[MeB(C_6F_5)_3]^-$ anion (see Fig. 6c, d and S13†). The relatively higher $\int\rho(r)\mathrm{d}r$ values found in the $[B(C_6F_5)_4]^-$ system are consistent with more numbers of F–H interactions at **2-TS3** (Fig. 4b). Overall, this NCI index, together with HOMO–LUMO gaps, further confirms the influence of weak (vdW) interactions in stabilising the propagating transition states *via* LUMO orbitals, with the third propagation showing the strongest one, and this may explain the reduced barriers observed in the third propagation of the cocatalyst systems.

4 Conclusions

A computational study of three model catalytic species, namely, methylzirconocene cation, Cp_2ZrMe^+, and two ion pairs of composition $[Cp_2ZrMe^+][A^-]$ (A^- = $[MeB(C_6F_5)_3]^-$ and $[B(C_6F_5)_4]^-$) and their CROP reaction with CL was carried out for the chain initiation, propagation, and termination mechanism. DFT calculations clearly show that the initiation is thermodynamically favoured for the CL insertion at the catalytic metal centre, whereas the propagation is kinetically controlled for successive insertion *via* CL ring-opening. The first two propagation steps, with relatively high and comparable barriers in the presence of the cocatalysts (79.2–80.6 and 73.9–78.2 kJ mol^{-1} for **1** and **2**), are likely the rate-determining steps of the CL CROP mechanism, and these data further verify the naked cation model applied in the literature,[60–62] including our previous studies.[53,63] The calculations support the cationic ACE mechanism with *O*-alkyl bond cleavage. Comparison of the first termination and the third propagation steps was also studied, and, with the exception of $[MeB(C_6F_5)_3]^-$, they are not competitive with the termination being less facile compared to the propagation step: the catalytic system **2** exhibits the more feasible termination over the system **1** when using methanol as a terminating agent. For most cases, the third propagation is found to be kinetically and thermodynamically favoured over the termination.

Despite the similar effect of the two counteranions on the reaction kinetics of CL CROP, the counteranion (A^-) stabilises the cationic species immediately after the first monomer insertion, and the $[MeB(C_6F_5)_3]^-$ anion effectively stabilises the catalyst–monomer complex more than the $[B(C_6F_5)_4]^-$ anion by ~24 kJ mol^{-1}. The anions greatly stabilises the terminating species after the first methanol insertion at the chain end. The NCI analysis reveals that the counteranions mainly participate in the reaction through weak interactions, with a distinct impact on the HOMO–LUMO gaps and transition-state stabilisation.

We also studied the initiation and propagation steps of the hafnocene catalyst, revealing that the Hf catalyst slightly favours

the CL CROP mechanism compared to the Zr catalyst. The effects of solvent and dispersion on the reaction energetics were analysed, demonstrating that both factors are crucial for the polymerisation. Overall, this study provides a comprehensive understanding of the CL CROP mechanism, revealing the influence of weak interactions at the contacts between the cationic species and the counteranions during chain initiation, propagation and termination.

Author contributions

Conceptualization: W. M., J. J.; investigation: W. M., J. J.; analysis and visualisation: J. J.; funding acquisition: J. J.; software: M. L., J. J.; supervision: M. L., J. J.; validation: M. L., J. J.; writing initial draft: W. M., J. J.; writing – review and editing: W. M., M. L., J. J.

Conflicts of interest

There are no conflicts to declare.

Acknowledgements

Financial supports of the Thailand Science Research and Innovation Fund and the University of Phayao (UP) under Fundamental Fund 2024 (Project No. 224/2567) and the School of Science, UP (Grant No. PBTSC66002 and PBTSC66023) are gratefully acknowledged. M. L. acknowledges the support of the Research Council of Finland, decision 357509.

References

1 P. R. Schmitt, K. D. Dwyer and K. L. K. Coulombe, *ACS Appl. Bio Mater.*, 2022, **5**, 2461–2480.
2 S. Espinoza, I. Patil, E. San Martín-Martínez, M. Martinez, R. Casañas Pimentel, P. Pradum, P. Ige, R. Pimentel and P. Ige, *Int. J. Polym. Mater. Polym. Biomater.*, 2020, **69**, 85–126.
3 T. Abudula, K. Gauthaman, A. Mostafavi, A. Alshahrie, N. Salah, P. Morganti, A. Chianese, A. Tamayol and A. Memic, *Sci. Rep.*, 2020, **10**, 20428.
4 K. Kaluzynski, J. Pretula, P. Lewinski, S. Kaźmierski and S. Penczek, *Macromolecules*, 2022, **55**, 2210–2221.
5 C. Jérôme and P. Lecomte, *Adv. Drug Delivery Rev.*, 2008, **60**, 1056–1076.
6 O. Nuyken and S. D. Pask, *Polymers*, 2013, **5**, 361–403.
7 O. Santoro, X. Zhang and C. Redshaw, *Catalysts*, 2020, **10**, 800.
8 M. Hong, J. Chen and E. Y. X. Chen, *Chem. Rev.*, 2018, **118**, 10551–10616.
9 D. M. Lyubov, A. O. Tolpygin and A. A. Trifonov, *Coord. Chem. Rev.*, 2019, **392**, 83–145.
10 L.-J. Wu, W. Lee, P. Kumar Ganta, Y.-L. Chang, Y.-C. Chang and H.-Y. Chen, *Coord. Chem. Rev.*, 2023, **475**, 214847.
11 S. Kaler and M. D. Jones, *Dalton Trans.*, 2022, **51**, 1241–1256.
12 R. A. Collins, A. F. Russell and P. Mountford, *Appl. Petrochem. Res.*, 2015, **5**, 153–171.
13 L. Resconi, L. Cavallo, A. Fait and F. Piemontesi, *Chem. Rev.*, 2000, **100**, 1253–1346.
14 Y. Nakayama and T. Shiono, *Molecules*, 2005, **10**, 620–633.
15 Y. Sarazin and J.-F. Carpentier, *Chem. Rev.*, 2015, **115**, 3564–3614.
16 M.-E. Kourti, E. Fega and M. Pitsikalis, *Polym. Chem.*, 2016, **7**, 2821–2835.
17 M.-E. Kourti, G. C. Vougioukalakis, N. Hadjichristidis and M. Pitsikalis, *J. Polym. Sci., Part A: Polym. Chem.*, 2011, **49**, 2520–2527.
18 E. Batagianni, A. Marathianos, A. Koraki, A.-P. Maroudas and M. Pitsikalis, *J. Macromol. Sci., Part A: Pure Appl. Chem.*, 2016, **53**, 140–151.
19 M. Hayakawa, M. Mitani, T. Yamada and T. Mukaiyama, *Macromol. Chem. Phys.*, 1997, **198**, 1305–1317.
20 K. Kostakis, S. Mourmouris, G. Karanikolopoulos, M. Pitsikalis and N. Hadjichristidis, *J. Polym. Sci., Part A: Polym. Chem.*, 2007, **45**, 3524–3537.
21 M. Hayakawa, M. Mitani, T. Yamada and T. Mukaiyama, *Macromol. Rapid Commun.*, 1996, **17**, 865–870.
22 S. Penczek, M. Cypryk, A. Duda, P. Kubisa and S. Słomkowski, *Prog. Polym. Sci.*, 2007, **32**, 247–282.
23 S. Penczek and J. Pretula, *ACS Macro Lett.*, 2021, **10**, 1377–1397.
24 T. Mukaiyama, M. Hayakawa, K. Oouchi, M. Mitani and T. Yamada, *Chem. Lett.*, 1995, **24**, 737–738.
25 Z. Ariffin, D. Wang and Z. Wu, *Macromol. Rapid Commun.*, 1998, **19**, 601–604.
26 M.-E. Kourti, G. Fotinogiannopoulou, E. Fega and M. Pitsikalis, *J. Macromol. Sci., Part A: Pure Appl.Chem.*, 2015, **52**, 630–641.
27 I. Nifant'ev and P. Ivchenko, *Molecules*, 2019, **24**, 4117.
28 J. Sassmannshausen, *Dalton Trans.*, 2009, 8993–8999.
29 G. Lanza and I. L. Fragalà, *Top. Catal.*, 1999, **7**, 45–60.
30 R. Parveen, T. R. Cundari, J. M. Younker and G. Rodriguez, *Organometallics*, 2020, **39**, 2068–2079.
31 W. Kohn and L. J. Sham, *Phys. Rev.*, 1965, **140**, A1133–A1138.
32 R. G. Parr and W. Yang, *Density-functional Theory of Atoms and Molecules*, Oxford University Press, 1994.
33 M. J. Frisch, G. W. Trucks, H. B. Schlegel, G. E. Scuseria, M. A. Robb, J. R. Cheeseman, G. Scalmani, V. Barone, B. Mennucci, G. A. Petersson, H. Nakatsuji, M. Caricato, X. Li, H. P. Hratchian, A. F. Izmaylov, J. Bloino, G. Zheng, J. L. Sonnenberg, M. Hada, M. Ehara, K. Toyota, R. Fukuda, J. Hasegawa, M. Ishida, T. Nakajima, Y. Honda, O. Kitao, H. Nakai, T. Vreven, J. A. Montgomery Jr, J. E. Peralta, F. Ogliaro, M. Bearpark, J. J. Heyd, E. Brothers, K. N. Kudin, V. N. Staroverov, T. Keith, R. Kobayashi, J. Normand, K. Raghavachari, A. Rendell, J. C. Burant, S. S. Iyengar, J. Tomasi, M. Cossi, N. Rega, J. M. Millam, M. Klene, J. E. Knox, J. B. Cross, V. Bakken, C. Adamo, J. Jaramillo, R. Gomperts, R. E. Stratmann, O. Yazyev, A. J. Austin, R. Cammi, C. Pomelli, J. W. Ochterski, R. L. Martin, K. Morokuma, V. G. Zakrzewski, G. A. Voth, P. Salvador, J. J. Dannenberg, S. Dapprich, A. D. Daniels, O. Farkas, J. B. Foresman,

J. V. Ortiz, J. Cioslowski, and D. J. Fox, *Gaussian 09*, Revision A.02, 2009.
34 Y. Yang, M. N. Weaver and K. M. Merz Jr, *J. Phys. Chem. A*, 2009, **113**, 9843–9851.
35 J. Jitonnom and W. Meelua, *Chem. Phys. Lett.*, 2020, **750**, 137482.
36 J. Jitonnom, R. Molloy, W. Punyodom and W. Meelua, *Comput. Theor. Chem.*, 2016, **1097**, 25–32.
37 J. Jitonnom and W. Meelua, *J. Theor. Comput. Chem.*, 2017, **16**, 1750003.
38 J. Jitonnom and W. Meelua, *Chiang Mai J. Sci.*, 2014, **41**(5.2), 1220–1229.
39 A. V. Marenich, C. J. Cramer and D. G. Truhlar, *J. Phys. Chem.*, 2009, **113**, 6378–6396.
40 S. Grimme, J. Antony, S. Ehrlich and H. Krieg, *J. Chem. Phys.*, 2010, **132**, 154104.
41 S. Grimme, S. Ehrlich and L. Goerigk, *J. Comput. Chem.*, 2011, **32**, 1456–1465.
42 J. Kumawat and V. K. Gupta, *ACS Catal.*, 2020, **10**, 1704–1715.
43 Y.-X. Chen, M. V. Metz, L. Li, C. L. Stern and T. J. Marks, *J. Am. Chem. Soc.*, 1998, **120**, 6287–6305.
44 S. Beck, M.-H. Prosenc, H.-H. Brintzinger, R. Goretzki, N. Herfert and G. Fink, *J. Mol. Catal. A: Chem.*, 1996, **111**, 67–79.
45 G. Luchini, J. Alegre-Requena, I. Funes-Ardoiz and R. Paton, *F1000Research*, 2020, **9**, 291.
46 M. Linnolahti and S. Collins, *Dalton Trans.*, 2022, **51**, 11152–11162.
47 M. Mammen, E. I. Shakhnovich, J. M. Deutch and G. M. Whitesides, *J. Org. Chem.*, 1998, **63**, 3821–3830.
48 E. R. Johnson, S. Keinan, P. Mori-Sánchez, J. Contreras-García, A. J. Cohen and W. Yang, *J. Am. Chem. Soc.*, 2010, **132**, 6498–6506.
49 R. Laplaza, F. Peccati, R. A. Boto, C. Quan, A. Carbone, J.-P. Piquemal, Y. Maday and J. Contreras-García, *Wiley Interdiscip. Rev.: Comput. Mol. Sci.*, 2021, **11**, e1497.
50 T. Novoa, R. Laplaza, F. Peccati, F. Fuster and J. Contreras-García, *J. Chem. Inf. Model.*, 2023, **63**, 4483–4489.
51 J. Contreras-García, E. R. Johnson, S. Keinan, R. Chaudret, J.-P. Piquemal, D. N. Beratan and W. Yang, *J. Chem. Theory Comput.*, 2011, **7**, 625–632.
52 W. Meelua, N. Keawkla, J. Oláh and J. Jitonnom, *J. Organomet. Chem.*, 2020, **905**, 121024.
53 J. Jitonnom and W. Meelua, *J. Organomet. Chem.*, 2017, **841**, 48–56.
54 A. Correa and L. Cavallo, *J. Am. Chem. Soc.*, 2006, **128**, 10952–10959.
55 L. Sian, A. Dall'Anese, A. Macchioni, L. Tensi, V. Busico, R. Cipullo, G. P. Goryunov, D. Uborsky, A. Z. Voskoboynikov, C. Ehm, L. Rocchigiani and C. Zuccaccia, *Organometallics*, 2022, **41**, 547–560.
56 F. Ruipérez, *Int. Rev. Phys. Chem.*, 2019, **38**, 343–403.
57 H. Goossens, S. Catak, M. Glassner, V. R. de la Rosa, B. D. Monnery, F. De Proft, V. Van Speybroeck and R. Hoogenboom, *ACS Macro Lett.*, 2013, **2**, 651–654.
58 Y. Cornaton and J.-P. Djukic, *Acc. Chem. Res.*, 2021, **54**, 3828–3840.
59 C. Uyeda and E. N. Jacobsen, *J. Am. Chem. Soc.*, 2011, **133**, 5062–5075.
60 A. Laine, B. B. Coussens, J. T. Hirvi, A. Berthoud, N. Friederichs, J. R. Severn and M. Linnolahti, *Organometallics*, 2015, **34**, 2415–2421.
61 S. Collins and M. Linnolahti, *ChemCatChem*, 2022, **14**, e202101918.
62 F. Zaccaria, C. Ehm, P. H. M. Budzelaar and V. Busico, *ACS Catal.*, 2017, **7**, 1512–1519.
63 W. Meelua, T. Wanjai and J. Jitonnom, *Sci. Rep.*, 2024, **14**, 3952.